CITATION

DOI

COPYRIGHT

USAGE

APPLYING THE
STEREOGRAPHIC PROJECTION
TO MODELING OF THE FLOW OF
THE ANTARCTIC CIRCUMPOLAR CURRENT

By Susanna V. Haziot and Kateryna Marynets

ABSTRACT. We discuss the use of stereographic projection for studying recent models of the flow of the Antarctic Circumpolar Current.

INTRODUCTION

For studies of large-scale oceanic flows, assuming a spherical Earth is appropriate because, while Earth's shape is that of an oblate sphere with an equatorial bulge, the difference between the equatorial and polar radii (about 22 km out of 7,378 km) is irrelevant (Constantin, 2012; Wunsch, 2015; Henry, 2018). Nevertheless, the equations governing fluid flow on a rotating sphere present considerable mathematical challenges, partly arising from effects of Earth's sphericity. For this reason, it is common in oceanographic studies to transform a specific geophysical flow problem into a simpler problem for planar flow, obtained from a suitable approximation. The commonly used approximations are the f-plane and β-plane approximations. If L is the length scale of the specific flow and R is Earth's radius, the f-plane equations are derived from the limit $L/R \rightarrow 0$ in the equations governing rotating spherical coordinates (Navier-Stokes equations if dissipative effects are accounted for and Euler equations for inviscid flows; see Grimshaw, 1975). The resulting equations are expressed in terms of Cartesian coordinates originating on Earth's surface (tangent plane approximations), and all terms associated with Earth's curvature are neglected. This makes the f-plane equation unsuitable for modeling large-scale ocean flows, so that the β-plane approximation is the basis for large-scale ocean dynamics.

The core idea of the β-plane approximation goes back to heuristic reasoning by Rossby (1939). Given that the average depth of the ocean is about 4 km, with the deepest point at 11 km in the Mariana Trench, Rossby argued that for a shallow fluid on a rotating sphere, only the local normal component of the angular velocity vector is relevant. Furthermore, if the scale of the motion is sufficiently small in the meridional direction, then the only effect of the sphericity to be retained is the variation of the normal component of the angular velocity with latitude (see the discussion in Drotos and Tel, 2015). These considerations lead to the β-plane equations, valid under the assumption of flat-space geometry with a linearly latitude-dependent angular velocity component (see Vallis, 2006). Despite being widely used, the β-plane equations do not provide a consistent approximation of the governing equations in non-equatorial regions (for a detailed discussion, see Dellar, 2011). Note that equatorial ocean dynamics exhibits features that are not encountered in mid-latitude flows or in flows at high latitudes. In particular, stratification is greater in equatorial regions than anywhere else in the ocean (Fedorov and Brown, 2009), and more importantly, the meridional component of the Coriolis force vanishes at the equator, implying that the equator works as a (fictitious) natural boundary, facilitating azimuthal flow propagation (see the discussions in Johnson et al., 2001; Constantin and Johnson, 2015, 2016a, 2017a; Henry, 2016). Thus, alternatives to the β-plane equations should be sought for studying large-scale non-equatorial ocean flows.

The Antarctic Circumpolar Current (ACC) is perhaps the most important flow of this type when considering global ocean circulation and global climate. The planet's most powerful current (Talley et al., 2011), the ACC isolates Antarctica from warm subtropical waters (see Figure 1). Situated roughly between 40°S and 60°S, the ACC is created by the action of very strong westerly winds combined with the Coriolis force. It transports about

140 million cubic meters of water per second, more than one hundred times the transport of all the world's rivers combined, over a distance of about 24,000 km. While the ACC does not exhibit high current velocities (the average surface velocity is about 30–40 cm s^{-1} within the Subantarctic and Polar Fronts; e.g., Firing et al., 2011), the current extends to the ocean floor (varying between 2 km and 4 km depth), where occasional irregular topographical features deflect the course of the flow from its predominantly zonal characteristic. Being the major means of exchange of water between the Atlantic, Pacific, and Indian ocean basins, the ACC plays an important role in global climate (Herbei et al., 2009).

Just as jet streams can form in atmospheric flows, oceanic flows are of sufficient spatial scale to spawn zonal jets (Sokolov and Rintoul, 2007). However, these jets are rare because landmasses typically interrupt their continuity. The ACC, being unobstructed by any land, is an exception to this general pattern. It is concentrated into several jets, typically about 40 km wide with speeds exceeding 1 m s^{-1}, that are separated by low-speed zones flowing at less than 20 cm s^{-1} (see the discussion in Constantin and Johnson, 2016b). As a measure of the might of the ACC flow, we note that in the southeast Atlantic Ocean, where the ACC meets the warm Agulhas current, it forces the

Agulhas to retroflect (turn back on itself; see Figure 2) so that it becomes the Agulhas Return Current, rejoining the Indian Ocean. This occurs despite the fact that the Agulhas current, flowing down the east coast of Africa from about 27°S to 40°S, is one of the ocean's strongest currents.

Due to the sheer size of the ACC, it is desirable to take the effects of Earth's sphericity into account while deriving models for its flow. The fundamental problem of cartography is that no map from the sphere to the plane can accurately represent both angles and areas. In general, area-preserving map projections are preferred for statistical applications, while angle-preserving (conformal) map projections are preferred for navigation. Stereographic projection falls into the second category and turns out to be quite useful for modeling ACC flow.
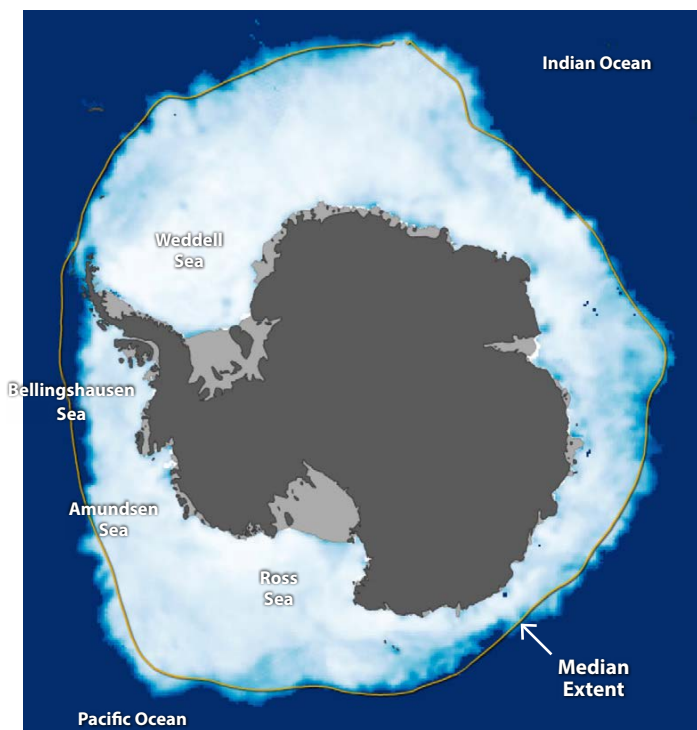

FIGURE 1. Map showing the sea ice extent around Antarctica on September 26, 2012, when ice, typically 1–2 m thick, covered more of the Southern Ocean than usual; almost all of the sea ice formed during the Antarctic winter melts during the summer. Because the Antarctic Circumpolar Current (ACC) isolates Antarctica from warmer waters to the north, ice forms in a nearly symmetric circular pattern around the South Pole. *Image credit: NASA Earth Observatory image by Jesse Allen, using DMPS SSMIS ice concentration data provided courtesy of the National Snow and Ice Data Center*
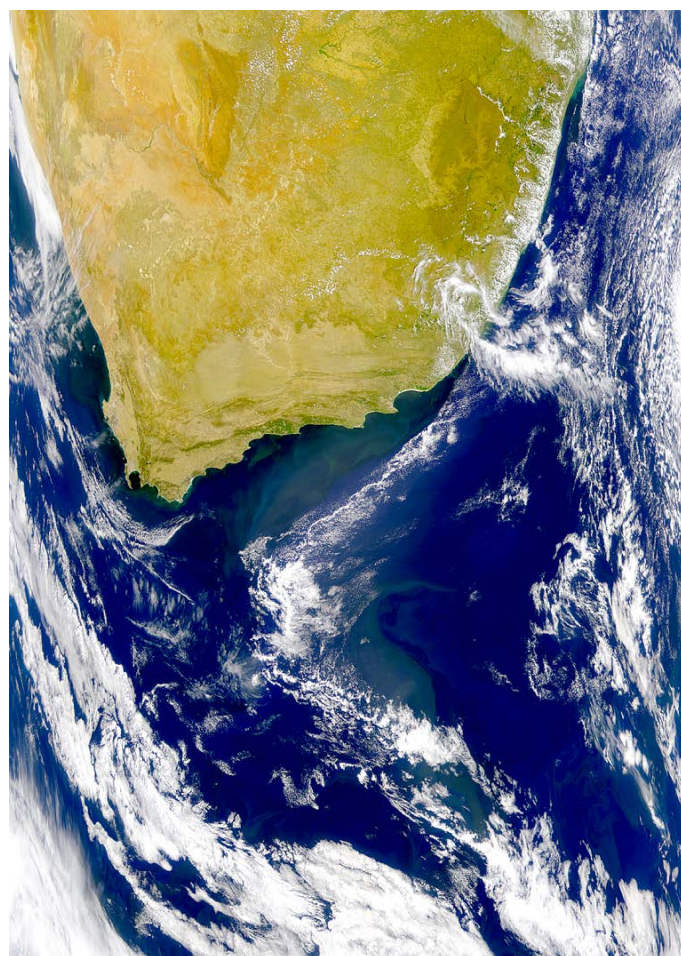

FIGURE 2. Satellite photograph showing the ocean region around the southern tip of Africa. While individual phytoplankton are tiny, when they bloom by the billions, resulting high concentrations of chlorophyll and other light-catching pigments change the way the surface reflects light and enhance visualization of flow patterns. Here, abundant phytoplankton help to delineate the current pattern in the region where the Agulhas current retroflection occurs—upon meeting the ACC, the Agulhas Current makes a nearly right-angled turn. These currents induce an upwelling of cold, nutrient-rich water from the deep, fertilizing the surface waters to create phytoplankton blooms in the open ocean, which is otherwise relatively barren compared to coastal waters. *Image credit: Provided by the SeaWiFS Project, NASA/Goddard Space Flight Center, and ORBIMAGE*

STEREOGRAPHIC PROJECTION

Stereographic projection, the oldest form of map projection, dates to the second century BCE (the oldest known record is from Ptolemy about 150 CE). It represents Earth's surface in two dimensions, which is projected from the observation point onto a plane parallel to the equatorial plane, typically the equatorial plane itself or a plane tangent to the sphere at the pole that is opposite to the pole from which the projection is done.

The benefits of stereographic projection are that Earth appears as if viewed from space and landmass shapes are generally well preserved, although extreme distortions occur toward the edge of the image created (Figure 3). Stereographic projection is particularly useful for plotting angular relationships because great circles are always arcs of circles and are easily constructed. Note that the lines of longitude and latitude are always orthogonal. When the projection is centered at Earth's North or South Pole, as is commonly the case, stereographic projection has additional desirable properties: meridians emanate in rays from the pole and in circles parallel to the pole, thus facilitating the mapping of astronomical observations. However, because the projection originates from the South or the North Pole, it cannot represent the surface of that territory. For this reason, stereographic projection is typically used for specific regions but rarely for maps of the world (Phillips, 1960; Leyshon and Lisle, 1996; Daners, 2012).

Images captured by geostationary satellites are important examples of stereographic projections. These images are centered at a point S on the equator (rather than at one of the poles, as in the previous discussion) and mapped onto the plane tangent to Earth at the point S′ on the equator, diametrically opposite S and located directly under the satellite. Geostationary satellites orbit Earth eastward above the equator at an altitude of about 35,790 km, so that their period equals the period of Earth's rotation. Thus, the satellite remains stationary above one point of the equator relative to Earth. Such a satellite is capable of scanning Earth up to 70° of latitude or longitude in each direction from the point S′, making regular sequential observations in the form of stereographic images. The imaging occurs in the visible and infrared parts of the light spectrum, commonly at resolutions of 1 km and 4 km, respectively. Among other applications, these satellites are used to monitor sensitive changes to ocean environments.

An alternative to stereographic projection is the Mercator projection (Figure 4). This projection, originating from the Flemish cartographer Gerardus Mercator in 1569, is the most used map in the world. It projects Earth from a sphere onto a plane. This projection has certain key characteristics: it preserves angles (hence, it is conformal), the north-south direction is the vertical direction, and the east-west direction is the horizontal direction. It does not, however, preserve areas: as the latitude increases from the equator, the size of objects is increasingly distorted to finally reach infinite scale at the poles. As a result, the world is mapped into an infinitely tall rectangle with constant width (see Daners, 2012).
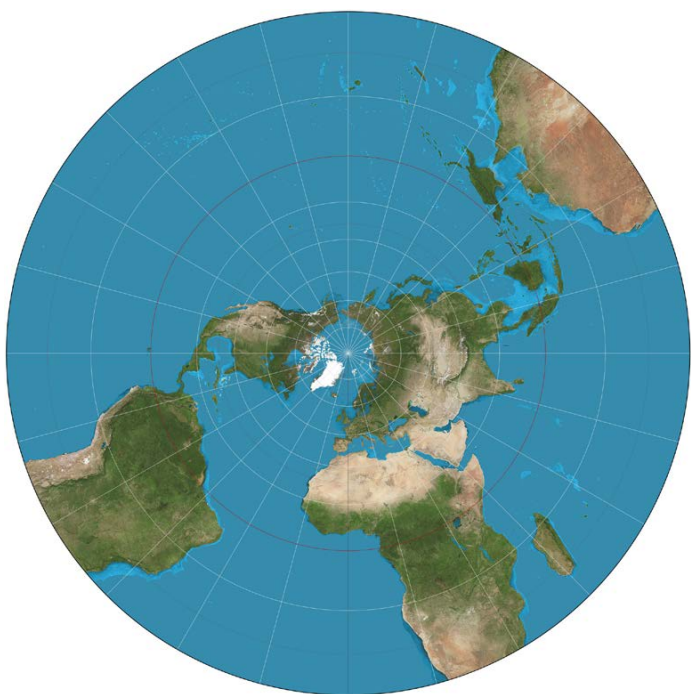

FIGURE 3. Stereographic projection of Earth from the South Pole to the plane tangent to the sphere at the North Pole. Increasing distance from the North Pole leads to increasing distortions, with the South Pole represented at an infinite distance *Image source: https://en.wikipedia.org/wiki/ File:Stereographic_projection_SW.JPG#filelinks*
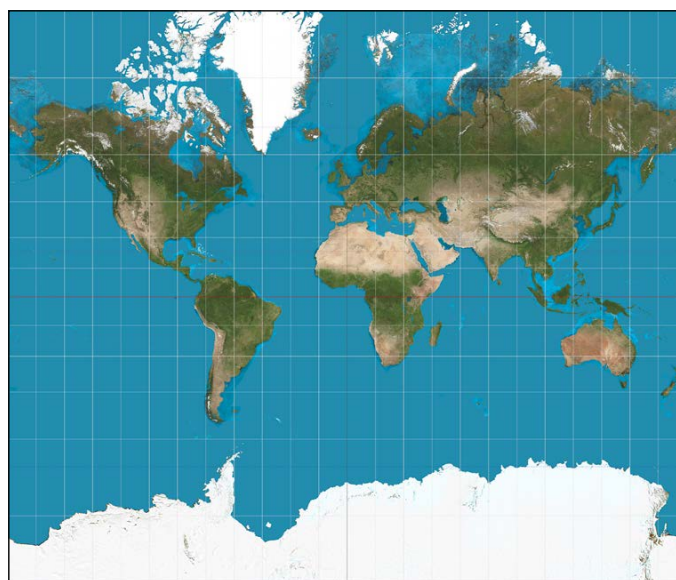

FIGURE 4. Mercator projection map of Earth. Mercator distortions are illustrated by comparing the sizes of Australia and Greenland: Australia is actually more than three times the size of Greenland. *Image source: https://commons.wikimedia.org/wiki/File:Mercator_projection_SW.jpg*

Stereographic projection of the unit sphere centered at origin, from the North Pole to the equatorial plane (Figure 5), is given by

$$\xi = r\,e^{i\phi} \quad \text{with} \quad r = \cot\left(\frac{\theta}{2}\right) = \frac{\sin\theta}{1-\cos\theta}, \tag{1}$$

where (r, ϕ) are the polar coordinates in the equatorial plane; here, $\theta \in (0, \pi)$ is the polar angle ($\frac{\pi}{2} - \theta$ being the angle of latitude) and $\phi \in [0, 2\pi)$ is the angle of longitude on the sphere. Every point P on the unit sphere is labeled by its spherical coordinates (θ, ϕ), with $\theta = 0$ corresponding to the North Pole, and $\theta = \frac{\pi}{2}$ to the equator.

In contrast, the Mercator projection is what is known as a cylindrical projection (Figure 6): a point P on the sphere is projected onto a point P' on the cylinder tangential to the sphere at the equator. Upon unrolling the cylinder, we then obtain a projection of the sphere onto the plane. This new plane has the equator as the x-axis and the central meridian as the y-axis, and all latitudes and longitudes are mapped onto the plane as straight lines parallel to the y- and to the x-axis, respectively (Figure 7). However, we want the map to be conformal, and therefore, we must have that the north-south distortion rate is the same as the east-west distortion rate. Because the radius of every parallel is given by $\sin(\theta)$, the corresponding parallel on the plane must be stretched by a factor of $\csc(\theta)$. Consequently, we slide P' down the generator of the cylinder to the point P'' (Figure 6) with coordinates

$$x = \phi, \quad y = \ln\left[\tan\left(\frac{\pi}{2} - \frac{\theta}{2}\right)\right].$$

Note that y tends to infinity at the poles (see the discussion in Daners, 2012).

MODELS OF THE ACC FLOW

The main driving force behind surface currents in the ocean is wind. Other factors such as topography, density differences caused by temperature and salinity variations, and the gravitational pull of the moon and sun also generate ocean currents. Horizontal currents represent the strongest large-scale ocean flows, and can have spatial scales of up to several hundreds of kilometers and temporal scales of many weeks to years (see Talley et al., 2011). These currents are deflected by the Coriolis force due to Earth's rotation, producing large-scale clockwise circular motions in the Northern Hemisphere and counterclockwise ones in the Southern Hemisphere. These large-scale circulating ocean currents form gyres that are found in every major ocean basin. Their movement drives what is referred to as the ocean conveyor belt, which in turn moves ocean water containing heat, chemicals, and nutrients around the planet.

Constantin and Johnson (2017b) derive a model for gyre flows in spherical coordinates by taking advantage of one of the fundamental properties of large-scale ocean flows: their vertical velocities are negligible with respect to the horizontal ones, being smaller by a factor of about 10^4. Because the ACC is a large-scale ocean current that makes a full circle around the globe, and the above property also applies, we study it by adapting its setting to the aforementioned approach in rotating spherical coordinates.

Consider spherical coordinates as in Figure 5, with $\theta \in [0, \pi)$ the polar angle and $\varphi \in [0, 2\pi)$ the angle of longitude. In terms of the stream function $\psi(\theta, \varphi)$, a horizontal ocean flow on the spherical Earth has azimuthal
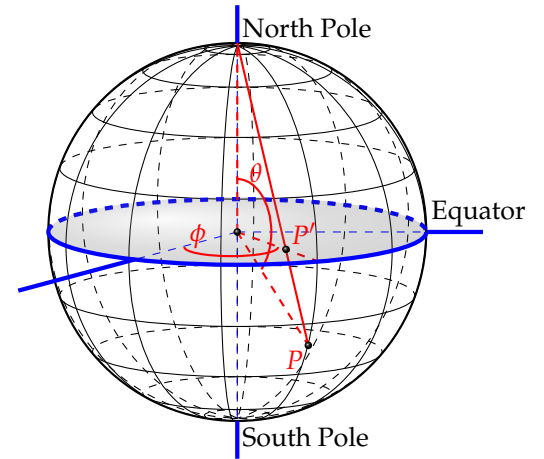
FIGURE 5. Stereographic projection of the unit sphere from the North Pole to the equatorial plane.
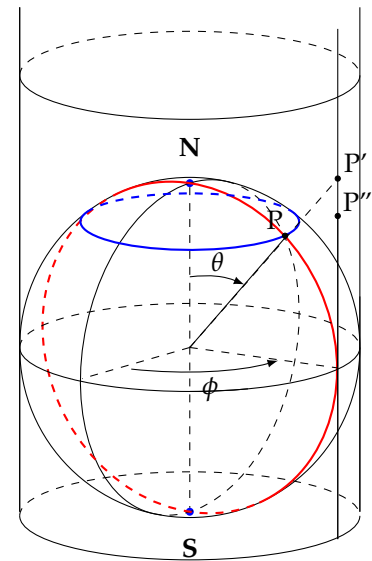
FIGURE 6. Mercator projection. The point P on the sphere is projected onto a point P' on the cylinder tangential to the sphere, that in turn slides down the cylinder to P'', the point at which the distortion rate is equal in both directions.
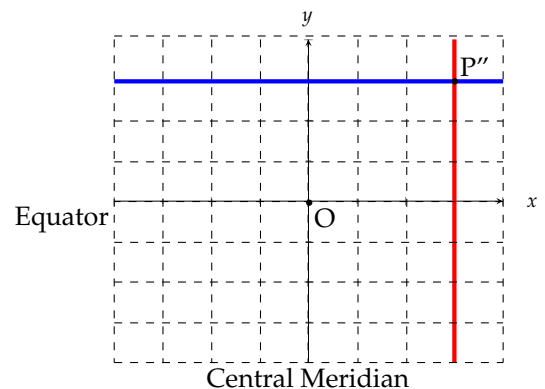
FIGURE 7. Unrolled cylinder.

and polar velocity components given by

$$\frac{1}{\sin\theta}\psi_\varphi \quad \text{and} \quad -\psi_\theta. \tag{2}$$

By associating $\Psi(\theta, \varphi)$ with the vorticity of the ocean motion (as distinct from the Earth's rotation), given by

$$\psi(\theta, \varphi) = -\omega \cos\theta + \Psi(\theta, \varphi), \tag{3}$$

where $\omega > 0$ is the nondimensional form of the Coriolis parameter, the governing equation for the horizontal flow on the sphere takes the form

$$\frac{1}{\sin^2\theta}\Psi_{\varphi\varphi} + \Psi_\theta \cot\theta + \Psi_{\theta\theta} = F(\Psi - \omega \cos\theta), \tag{4}$$

in which the term $F(\Psi - \omega \cos\theta)$ is the oceanic vorticity and $2\omega \cos\theta$ is the planetary vorticity generated by the rotating Earth (see Constantin and Johnson, 2017b). The (total) vorticity of a geophysical fluid flow is the sum of the oceanic vorticity contribution $F(\Psi - \omega \cos\theta)$ and of the spin vorticity contribution $2\omega \cos\theta$, the oceanic vorticity F being typically one order of magnitude larger than $\omega > 0$. While the planetary vorticity is prescribed, the oceanic vorticity depends on the type of geophysical flow that is under consideration, for example $F \equiv 0$ for irrotational flow fields.

With exception of tidal currents (flood and ebb; see discussion in Constantin, 2011), the main source of oceanic vorticity is the wind. Both these types of oceanic vorticities can be modeled as non-zero constants (Da Silva and Peregrine, 1988; Ewing, 1990; Constantin et al., 2016) that may be positive or negative, depending on the prevalent wind direction, and on whether the flow is in an ebb or flood tidal mode, respectively. However, nonconstant oceanic vorticities are more realistic, even if the mathematical complexity of the problem is increased. Note that the strongest average surface winds of any open ocean area in the world blow over the Southern Ocean, with an annual average wind speed of about 28–45 km h^{-1} (Yuan, 2004; Smith et al., 2018). Therefore, it is expected that surface wave-current interactions in the Southern Ocean will give rise to intricate wave patterns, some of which are not fully elucidated (see the discussion in Constantin and Monismith, 2017). Also, in certain areas of the Southern Ocean, for example, at the southern tip of Africa, wave heights in excess of 35 m occur quite frequently (Walton, 2013). For discussions of analytical aspects of waves propagating at the surface of water in a flow with underlying non-uniform currents, see Henry (2013) and Constantin et al., (2016); also see Da Silva and Peregrine (1988), Thomas (1990), and Moreira and Chacaltana (2015) for numerical simulations, and Ewing (1990) and Constantin (2011) for field data. The stereographic and Mercator projections permit us to transform the model (4) for the horizontal ocean flow in spherical coordinates into a planar elliptic partial differential equation with appropriate boundary conditions.

Using Stereographic Projection

The region of the Southern Ocean where the ACC flows is mapped by a stereographic projection from the North Pole into an annular region $\mathcal{O}$ of the equatorial plane, given by

$$\mathcal{O} = \{(x, y): \ r_- < r = \sqrt{x^2 + y^2} < r_+\} \tag{5}$$

for suitable constants r_1 and r_2 with $0 < r_- < r_+ < 1$, because circles of latitude in the Southern Hemisphere are mapped into concentric circles contained within the unit circle of the equatorial plane.

Equation (4) is transformed into

$$\psi_{\xi\bar{\xi}} + 2\omega \frac{1 - \xi\bar{\xi}}{(1 + \xi\bar{\xi})^3} - \frac{F(\psi)}{(1 + \xi\bar{\xi})^2} = 0,$$

which, in terms of the Cartesian coordinates (x, y) in the complex ξ-plane, is equivalent to the semilinear elliptic equation

$$\Delta\psi + 8\omega \frac{1 - (x^2 + y^2)}{(1 + x^2 + y^2)^3} - \frac{4F(\psi)}{(1 + x^2 + y^2)^2} = 0, \tag{6}$$

where $\Delta = \partial_x^2 + \partial_y^2$ is the Laplace operator. The horizontal flow is determined in the new coordinates by the solution to (6) inside the planar region delimited by two level sets of the stream function, so that (6) has to be solved in a planar region O with Dirichlet boundary data.

A flow with no variation in the azimuthal direction, a feature that the ACC presents at leading order, corresponds to a radially symmetric solution, $\psi = \psi(r)$, of the problem (6). With

$$0 < t_1 = -\ln(r_+) < t_2 = -\ln(r_-),$$

the change of variables $r = e^{-t/2}$ and

$$\psi(r) = u(t), \qquad t_1 < t < t_2, \tag{7}$$

transforms the partial differential equation (6) to the second-order ordinary differential equation

$$u''(t) - \frac{e^t}{(1 + e^t)^2} F(u(t)) + \frac{2\omega e^t(1 - e^t)}{(1 + e^t)^3} = 0 \tag{8}$$

for $t_1 < t < t_2$, with associated boundary conditions

$$\begin{cases} u(t_1) = \alpha_1, \\ u(t_2) = \alpha_2, \end{cases} \tag{9}$$

expressing the fact that $r = r_\pm$ are streamlines, with $\psi = \alpha_1$ on $r = r_-$ and $\psi = \alpha_2$ on $r = r_+$.

In the case of linear stream functions F, some explicit solutions of the boundary-value problem (8), (9) can be obtained; see (Marynets, 2017a; Marynets, 2017b). Some of these results follow.

For

$$F(u, t) = p(t)u + q(t), \tag{10}$$

where $p, q : [t_1, t_2] \to \mathbb{R}$ are continuous functions, the differential equation (8) can be written as

$$\begin{cases} u''(t) - a(t)\,u(t) = b(t), & t_1 < t < t_2\,, \\ u(t_1) = \alpha_1\,, \\ u(t_2) = \alpha_2\,, \end{cases} \qquad (11)$$

where

$$a(t) := \frac{p(t)\,e^t}{(1+e^t)^2}\,, \qquad b(t) := \frac{q(t)\,e^t}{(1+e^t)^2} - \frac{2\omega e^t(1-e^t)}{(1+e^t)^3}$$

for $t \in [t_1, t_2]$.

The boundary-value problem (11) has a unique solution if and only if the associated homogeneous boundary-value problem,

$$\begin{cases} u''(t) - a(t)\,u(t) = 0, & t_1 < t < t_2\,, \\ u(t_1) = u(t_2) = 0, \end{cases} \qquad (12)$$

has only a trivial solution. Indeed, if $\{u_1(t), u_2(t)\}_{t \in [t_1, t_2]}$ is a fundamental system of solutions of the second-order differential equation in (12), and if $u_0(t)$ is a particular solution of the differential equation in (11), then the general solution of the differential equation in (11) has the form

$$u(t) = u_0(t) + c_1 u_1(t) + c_2 u_2(t), \qquad (13)$$

$t \in [t_1, t_2]$, for some constants $c_1, c_2 \in \mathbb{R}$. Using this general result, we consider some examples:

EXAMPLE 1

If $F \equiv 0$, then the general solution (13) of the differential equation

$$u''(t) + \frac{2\omega e^t(1-e^t)}{(1+e^t)^3} = 0,$$

is given by the formula

$$u(t) = c_1 + c_2 t + \omega \tanh(t/2) + q\,\ln(1+e^t),$$

$t \in (t_1, t_2)$, where c_1 and c_2 are some suitably chosen constants that accommodate the two–point boundary conditions in (11).

EXAMPLE 2

For $F(u) = -2u$, the differential equation has the form of

$$u'' + \frac{2e^t}{(1+e^t)^2}\,u + \frac{2\omega e^t(1-e^t)}{(1+e^t)^3} = 0,$$

and the explicit solution is given by expression

$$u(t) = \frac{2\omega}{3}\,\tanh(t/2)\,\ln[\cosh(t/2)]$$
$$+\, c_1\,\tanh(t/2) + c_2\Big(2 - t\tanh(t/2)\Big)$$

for which the constants c_1 and c_2 are chosen to accommodate the two boundary conditions in (11).

We also observe that since (1) yields

$$u'(t) = -\frac{1}{2}\,r\,\psi_r = -\frac{1}{2}\,\psi_\theta\,\sin\theta\,,$$

and $\sin\theta \in (0, 1)$ throughout the Southern Ocean, (2) shows

that the flow in a jet component of the ACC, between the parallels of latitude defined by an appropriate choice of $r_\pm \in (0, 1)$, is modeled by coupling the differential equation (8) with the boundary conditions

$$u'(t_1) = u'(t_2) = 0\,. \qquad (14)$$

which express the fact that there is no flow across the boundary of the jet. The boundary value problem (8)–(14) is therefore a model for a jet component of the ACC (see Marynets, 2017c).

Using the Mercator Projection

In this section, in order for our final partial differential equation to be easier to work with, rather than projecting our governing equation onto the sphere using the Mercator projection as described in the Stereographic Projection section, we instead map the latitudes onto the x-axis and the longitude onto the y-axis. In other words, we use the change of variables,

$$x = -\ln\left[\tan\left(\frac{\theta}{2}\right)\right], \qquad y = \varphi, \qquad (15)$$

so that our rectangle, which is now rotated by 90°, is infinite in the x-axis with constant width of 2π in the y-axis. As a result, the North Pole ($\theta = 0$) corresponds to $x = -\infty$ and the equator ($\theta = \frac{\pi}{2}$) to $x = 0$.

Using the change of variables (15), x is positive in the Southern Hemisphere, with

$$\cos(\theta) = \tanh(x), \qquad \sin(\theta) = \cosh^{-1}(x)\,.$$

Setting

$$u(x, y) = \psi(\theta, \varphi),$$

we can then rewrite the governing equation (4) as the following semilinear elliptic partial differential equation

$$\triangle u(x, y) = \frac{F(u(x, y))}{\cosh^2(x)} + 2\omega\frac{\sinh(x)}{\cosh^3(x)}\,. \qquad (16)$$

Because the ACC is situated between the 40th and 60th parallels, which we can denote by θ_1 and θ_2, we obtain the following two-point boundary conditions:

$$u(x_1, y) = u_1(y), \qquad x = x_1 > 0\,, \qquad (17)$$

$$u(x_2, y) = u_2(y), \qquad x = x_2 > 0\,, \qquad (18)$$

given that the boundary of the relevant region on the sphere corresponds to the parallels $\theta_1 = 2\arctan(e^{-x_1}) \in (\frac{\pi}{2}, \pi)$ and $\theta_2 = 2\arctan(e^{-x_2}) \in (\frac{\pi}{2}, \pi)$ situated in the Southern Hemisphere (see Figure 8).

For constant and linear oceanic vorticities, setting $F(u) = \gamma$ and $F(u) = au + b$ with $\gamma, a, b \in \mathbb{R}$, respectively, we can use a variational approach to study (16). Let us denote our domain $[x_1, x_2] \times [0, 2\pi)$ in the plane by Ω. Existence of weak solutions to (16) on Ω can be shown using the Lax-Milgram theorem, and regularity is then recovered using the regularity theorems for

elliptic partial differential equations (see Brezis, 2010). In particular, because $f(x) := 2\omega \frac{\sinh(x)}{\cosh^3(x)} \in C^\infty(\overline{\Omega})$, the solution u is smooth. Using the maximum principle for elliptic partial differential equations, uniqueness of solutions to (16) can then be recovered, except in the linear case for certain specific negative $a \in \mathbb{Z}$ (for details, see Haziot, in press).

Because u is periodic in the y-variable, we can expand u as a Fourier series in y with coefficients that depend on the x-variable. For linear F, using the method of separation of variables, the linear elliptic partial differential equation reduces to an infinite number of boundary-value problems for second-order ordinary differential equations. These in turn can then be solved to obtain explicit solutions for special oceanic vorticities (see Haziot, in press).

For example, for constant vorticity of the form $F(u) = \gamma$, with $\gamma \in \mathbb{R}$,

$$u(x,y) = \sum_{k \in \mathbb{Z}, k \leq -2} \alpha_k e^{iky} e^{k(x_0 - x)} + \sum_{k \in \mathbb{Z}, k \geq 2} \alpha_k e^{iky} e^{k(x - x_0)}$$

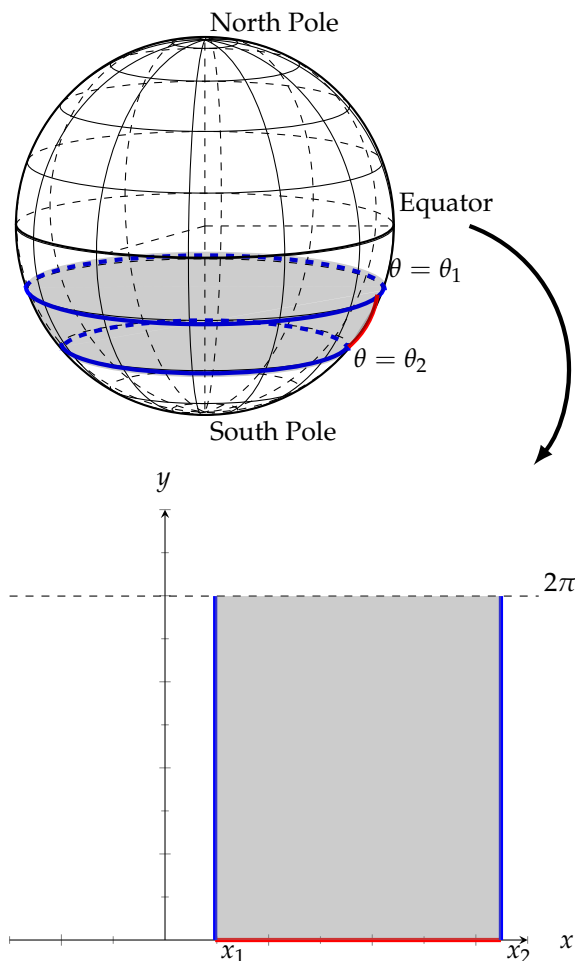$$+ \gamma[x + \ln(2\cosh(x))] - \omega[1 + \tanh(x)]$$

FIGURE 8. Mercator projection for the ACC. The polar angle is projected onto the x-axis and the azimuthal angle onto the y-axis. The South Pole is situated at $x = \infty$.

is a general solution to (16) with boundary conditions (17) and (18). There are no solutions for $\alpha_1 \neq 0$ or for $\alpha_{-1} \neq 0$, the modes $k = \pm 1$ being resonant.

For linear vorticities of the form $F(u) = au + b$, with $a = -l(l+1), l \in \mathbb{R}$ and $b \in \mathbb{R}$,

$$u(x,y) = \sum_{k \in \mathbb{Z}^*, |k| \leq l} \alpha_k [P_l^k(\tanh(x_0))]^{-1} P_l^k(\tanh(x)) e^{iky}$$

$$+ b[x + \ln(2\cosh(x))] - \omega[1 + \tanh(x)]$$

is the general solution to (16) with boundary conditions (17) and (18) where $P_l^k(z)$ is known as the associated Legendre function for $k \in \mathbb{R} \setminus \mathbb{Z}$ and the associated Legendre polynomials for $k \in \mathbb{Z}$. For more details on these special functions, see Abramowitz and Stegun (1964) and G. Andrews (1999).

CONCLUSIONS

We showed that the stereographic projection and the Mercator projection can be applied to study the ACC flow in spherical coordinates. Using these projections leads us to simple ACC models in the form of specific planar boundary-value problems for elliptic partial differential equations, which admit explicit solutions. The described procedure permits us to treat the ACC globally, taking into account the effects of Earth's sphericity. By increasing the complexity of the model (e.g., by permitting azimuthal variations and by considering more intricate expressions for the oceanic vorticity), the procedure implemented in this paper can incorporate details that increase accuracy. The main advantage is in the possibility of pursuing studies in flat-space for large-scale phenomena on a rotating sphere without the restriction associated with the use of the f-plane approximation and overcoming the inconsistencies associated with the use of the β-plane approximation in non-equatorial regions. ⓒ

REFERENCES

Abramowitz, M., and I. Stegun, eds. 1964. *Handbook of Mathematical Functions with Formulas, Graphs, and Mathematical Tables*. Cambridge University Press, Cambridge, 1,046 pp.

Andrews, G.E., R. Askey, and R. Roy. 1999. *Special Functions*. Cambridge University Press, Cambridge, 682 pp.

Brezis, H. 2010. *Functional Analysis, Sobolev Spaces, and Partial Differential Equations*. Springer, 600 pp.

Constantin, A. 2011. *Nonlinear Water Waves with Applications to Wave-Current Interactions and Tsunamis*. CBMS-NSF Regional Conference Series in Applied Mathematics, vol. 81, Society for Industrial and Applied Mathematics (SIAM), Philadelphia, PA, https://doi.org/10.1137/1.9781611971873, 323 pp.

Constantin, A. 2012. An exact solution for equatorially trapped waves. *Journal of Geophysical Research* 117, C05029, https://doi.org/10.1029/2012JC007879.

Constantin, A., and R.S. Johnson. 2015. The dynamics of waves interacting with the Equatorial Undercurrent. *Geophysical & Astrophysical Fluid Dynamics* 109:311–358, https://doi.org/10.1080/03091929.2015.1066785.

Constantin, A., and R.S. Johnson. 2016a. An exact, steady, purely azimuthal equatorial flow with a free surface. *Journal of Physical Oceanography* 46:1,935–1,945, https://doi.org/10.1175/JPO-D-15-0205.1.

Constantin, A., and R.S. Johnson. 2016b. An exact, steady, purely azimuthal flow as a model for the Antarctic Circumpolar Current. *Journal of Physical Oceanography* 46:3,585–3,594, https://doi.org/10.1175/JPO-D-16-0121.1.

Constantin, A., and R.S. Johnson. 2017a. A nonlinear, three-dimensional model for ocean flows, motivated by some observations of the Pacific equatorial undercurrent and thermocline. *Physics of Fluids* 29, 056604, https://doi.org/10.1063/1.4984001.

Constantin, A., and R.S. Johnson. 2017b. Large gyres as a shallow-water asymptotic solution of Euler's equation in spherical coordinates. *Proceedings of the Royal Society A* 473, https://doi.org/10.1098/rspa.2017.0063.

Constantin, A., and S.G. Monismith. 2017. Gerstner waves in the presence of mean currents and rotation. *Journal of Fluid Mechanics* 820:511–528, https://doi.org/10.1017/jfm.2017.223.

Constantin, A., W. Strauss, and E. Varvaruca. 2016. Global bifurcation of steady gravity water waves with critical layers. *Acta Mathematica* 217:195–262, https://doi.org/10.1007/s11511-017-0144-x.

Daners, D. 2012. The Mercator and stereographic projections, and many in between. *The American Mathematical Monthly* 119:199–210, https://doi.org/10.4169/amer.math.monthly.119.03.199.

Da Silva, A.F.T., and D.H. Peregrine. 1988. Steep, steady surface waves on water of finite depth with constant vorticity. *Journal of Fluid Mechanics* 195:281–302, https://doi.org/10.1017/S0022112088002423.

Dellar, P.J. 2011. Variations on a beta-plane: Derivation of non-traditional beta-plane equations from Hamilton's principle on a sphere. *Journal of Fluid Mechanics* 674:174–195, https://doi.org/10.1017/S0022112010006464.

Drotos, G., and T. Tel. 2015. On the validity of the β-plane approximation in the dynamics and the chaotic advection of a point vortex pair model on a rotating sphere. *Journal of the Atmospheric Sciences* 79:415–429, https://doi.org/10.1175/JAS-D-14-0101.1.

Ewing, J.A. 1990. Wind, wave and current data for the design of ships and off-shore structures. *Marine Structures* 3:421–459, https://doi.org/10.1016/0951-8339(90)90001-8.

Fedorov, A.V., and J.N. Brown. 2009. Equatorial waves. Pp. 3,679–3,695 in *Encyclopedia of Ocean Sciences*. J. Steele, ed., Academic Press, San Diego.

Firing, Y.L., T.K. Chereskin, and M.R. Mazloff. 2011. Vertical structure and transport of the Antarctic Circumpolar Current in Drake Passage from direct velocity observations. *Journal of Geophysical Research* 116, C08015, https://doi.org/10.1029/2011JC006999.

Grimshaw, R.H.J. 1975. A note on the β-plane approximation. *Tellus* 27:351–357, https://doi.org/10.3402/tellusa.v27i4.9982.

Haziot, S.V. In press. Study of an elliptic partial differential equation modeling the Antarctic Circumpolar Current. *Discrete and Continuous Dynamical Systems*.

Henry, D. 2013. Large amplitude steady periodic waves for fixed-depth rotational flows. *Communications in Partial Differential Equations* 38:1,015–1,037, https://doi.org/10.1080/03605302.2012.734889.

Henry, D. 2016. Equatorially trapped nonlinear water waves in a β-plane approximation with centripetal forces. *Journal of Fluid Mechanics* 804, R1, https://doi.org/10.1017/jfm.2016.544.

Henry, D. 2018. On three-dimensional Gerstner-like equatorial water waves. *Philosophical Transactions of the Royal Society A* 376(211), https://doi.org/10.1098/rsta.2017.0088.

Herbei, R., I. McKeague, and K.G. Speer. 2009. Gyres and jets: Inversion of tracer data for ocean circulation structure. *Journal of Physical Oceanography* 39:1,180–1,202, https://doi.org/10.1175/2007JPO3835.1.

Johnson, G.C., M.J. McPhaden, and E. Firing. 2001. Equatorial Pacific Ocean horizontal velocity, divergence, and upwelling. *Journal of Physical Oceanography* 31(3):839–849, https://doi.org/10.1175/1520-0485(2001)031<0839:EPOHVD>2.0.CO;2.

Leyshon, P.R., and R.J. Lisle. 1996. *Stereographic Projection Techniques in Structural Geology*. Butterworth–Heinemann Ltd, 121 pp.

Marynets, K. 2017a. A nonlinear two-point boundary value problem in geophysics. *Monatshefte für Mathematik*, https://doi.org/10.1007/s00605-017-1127-x.

Marynets, K. 2017b. On a two-point boundary-value problem in geophysics. *Applicable Analysis*, https://doi.org/10.1080/00036811.2017.1395869.

Marynets, K. 2017c. Weighted Sturm-Liouville problem related to ocean flows. *Journal of Mathematical Fluid Mechanics*, https://doi.org/10.1007/s00021-017-0347-0.

Moreira, R.M., and J.T.A. Chacaltana. 2015. Vorticity effects on nonlinear wave-current interactions in deep water. *Journal of Fluid Mechanics* 778:314–334, https://doi.org/10.1017/jfm.2015.385.

Phillips, F.C. 1960. *The Use of Stereographic Projection in Structural Geology*, 2nd ed. Edward Arnold Ltd., 86 pp.

Rossby, C.-G. 1939. Relation between variations in the intensity of the zonal circulation of the atmosphere and the displacements of the semi-permanent centers of action. *Journal of Marine Research* 27:38–55.

Smith, R., M. Desflots, S. White, A.J. Mariano, and E.H. Ryan. 2018. Surface currents in the Southern Ocean: The Antarctic CP Current, http://oceancurrents.rsmas.miami.edu/southern/antarctic-cp.html.

Sokolov, S., and S. Rintoul. 2007. Multiple jets of the Antarctic Circumpolar Current south of Australia. *Journal of Physical Oceanography* 37:1,394–1,412, https://doi.org/10.1175/JPO3111.1.

Talley, L.D., G.L. Pickard, W.J. Emery, and J.H. Swift. 2011. *Descriptive Physical Oceanography: An Introduction*. Academic Press, 560 pp.

Thomas, G.P. 1990. Wave-current interactions: An experimental and numerical study. *Journal of Fluid Mechanics* 216:505–536, https://doi.org/10.1017/S0022112081000839.

Vallis, G.K. 2006. *Atmospheric and Oceanic Fluid Dynamics*. Cambridge University Press.

Walton, D.W.H., ed. 2013. *Antarctica: Global Science from a Frozen Continent*. Cambridge University Press, Cambridge, 352 pp.

Wunsch, C. 2015. *Modern Observational Physical Oceanography*. Princeton University Press, New Jersey, 512 pp.

Yuan, X. 2004. High-wind-speed evaluation in the Southern Ocean. *Journal of Geophysical Research* 109, D13101, https://doi.org/10.1029/2003JD004179.

ACKNOWLEDGMENTS

AUTHORS' CONTRIBUTIONS

The authors contributed equally to this study.

AUTHORS

Susanna V. Haziot (susanna.haziot@univie.ac.at) and **Kateryna Marynets** (kateryna.marynets@univie.ac.at) are researchers at the Faculty of Mathematics, University of Vienna, Austria.

ARTICLE CITATION